Journal of Materials Chemistry A

PAPER

View Article Online
View Journal | View Issue

Cite this: J. Mater. Chem. A, 2015, 3, 19545

Advanced asymmetric supercapacitors based on CNT@Ni(OH)$_2$ core–shell composites and 3D graphene networks†

Huan Yi,[a] Huanwen Wang,[a] Yuting Jing,[a] Tianquan Peng,[a] Yiran Wang,[b] Jiang Guo,[b] Qingliang He,[b] Zhanhu Guo*[b] and Xuefeng Wang*[a]

Received 7th August 2015
Accepted 17th August 2015

DOI: 10.1039/c5ta06174a

www.rsc.org/MaterialsA

Asymmetric supercapacitors (ASCs) with carbon nanotube@nickel hydroxide nanosheet (CNT@Ni(OH)$_2$) core–shell composites as positive electrodes and three-dimensional (3D) graphene networks (3DGNs) as negative electrodes were reported in aqueous KOH electrolyte. The CNT@Ni(OH)$_2$ core–shell composites were prepared through a facile chemical bath deposition method, while 3DGNs were obtained by freeze-drying of graphene hydrogels. By virtue of their unique microstructures, superb electrochemical properties were achieved in a three-electrode system, *e.g.*, 1136 F g^{-1} at 2 A g^{-1} for the CNT@Ni(OH)$_2$ electrode within 0–0.5 V and 203 F g^{-1} at 1 A g^{-1} for the 3DGN electrode within −1–0 V. Benefiting from these merits, the as-fabricated CNT@Ni(OH)$_2$//3DGN ASC showed a maximum energy density of 44.0 W h kg^{-1} at a power density of 800 W kg^{-1} and even retained 19.6 W h kg^{-1} at 16 000 W kg^{-1} in the voltage region of 0–1.6 V.

1. Introduction

In response to the environmental problems and the energy crisis, there is an urgent need to develop clean, efficient and renewable sources of energy, as well as new technologies associated with energy conversion and storage.[1] Among various energy storage devices, supercapacitors have attracted intense research attention due to their higher energy density than conventional dielectric capacitors and higher power density than batteries along with a fast charging–discharging rate and exceptionally long cycle life.[1–5] Unfortunately, the energy density of supercapacitors (usually less than 10 W h kg^{-1}) is much lower than that of conventional batteries, which hinders their widespread applications in energy storage.[6] To improve the energy density (E) of supercapacitors, many research efforts have been made towards maximizing the specific capacitance (C) and/or the operating potential window (V) according to the equation: $E = 0.5CV^2$. Non-aqueous electrolytes (organic and ionic liquids) can extend the potential window up to 3 V; nevertheless, non-aqueous electrolytes suffer from poor ionic conductivity, flammability and high cost.[6,7] Recently, constructing asymmetric supercapacitors (ASCs) in aqueous electrolytes has been a promising alternative due to the high ionic conductivity, low cost, and "green" nature (environmental friendliness) of aqueous electrolytes.[4–10] These ASCs usually consist of a battery-like faradic electrode (as the energy source) and a capacitive electrode (as the power source), which can make full use of different operating voltages of the two electrodes to extend the potential window for the whole system. In order to boost the performance of the ASCs, selecting materials with judiciously designed structures for positive and negative electrodes becomes the prerequisite.

Hitherto, a range of materials such as transition metal oxides, metal hydroxides, and electronically conducting polymers have been reported and studied as positive electrodes in ASCs because of their high redox-acitivity.[5,7,11] Among them, nickel hydroxide is an attractive one due to its high specific capacitance, low cost and various morphologies.[4,5,12–14] However, the poor electronic conductivity of nickel hydroxide significantly hinders electron transport and decelerates the redox reactions, resulting in poor rate capability. To deal with this issue, the commonly used strategy is combining the nanosized Ni(OH)$_2$ with electrically conductive frameworks, such as carbon nanotubes (CNTs),[4,15–17] activated carbon,[18,19] graphene,[20–23] graphene foam[24] and Ni foam.[25,26] Among these options, CNTs are particularly viable for their excellent conductivity, high specific surface area, high strength, chemical stability and low density.[27–29] Although the previously reported CNT-supported Ni(OH)$_2$ composites have already shown enhanced pseudocapacitive performance, directly growing ultrathin and interleaving Ni(OH)$_2$ nanosheets vertically on

[a]Department of Chemistry, and Shanghai Key Lab of Chemical Assessment and Sustainability, Tongji University, Shanghai 200092, China. E-mail: xfwang@tongji.edu.cn

[b]Integrated Composites Laboratory (ICL), Department of Chemical & Biochemical Engineering, University of Tennessee, Knoxville, TN 37996, USA. E-mail: zguo10@utk.edu

† Electronic supplementary information (ESI) available. See DOI: 10.1039/c5ta06174a

CNTs with high mass by a facile method still remains a challenging task.

Regarding the negative electrode materials in ASCs, carbon materials that possess high specific surface area and good electrical conductivity are mostly used.[1,7] Although an extended potential window can be realized in ASCs, the cell capacitance (C_T) is limited by the lower capacitance electrode, usually the capacitance of the negative carbon electrode material (C_-), according to the relation: $1/C_T = 1/C_+ + 1/C_-$.[1,30] Thus, to obtain high capacitance and high energy density ASCs, carbon materials with optimized pore structure and high capacitance performance are urgent requisites. In this context, graphene, a single-atom-thick sheet of hexagonally arrayed sp^2-bonded carbon atoms, has emerged as a promising candidate for supercapacitor electrode materials due to its high theoretical specific surface area ($\sim$2600 m^2 g^{-1}), outstanding electrical conductivity, good chemical stability, and high mechanical strength.[31,32] However, due to inter-sheet van der Waals interactions, the aggregation or restacking of graphene sheets usually occurring during the synthesis and electrode preparation procedures will reduce the effective surface area and consequently hinder the ion diffusion from the electrolyte to the electrodes, which reduces the effective capacitance.[33,34] Very recently, some studies have shown that graphene oxide (GO) can form three-dimensional (3D) porous structures such as graphene hydrogels or aerogels, which would effectively prevent the restacking of graphene sheets and maintain their high specific surface area.[35–38] Moreover, such 3D porous graphene networks can ensure multi-dimensional electron transport pathways, ease access to the electrolyte, and minimize transport distances between the bulk electrode and the electrolyte, which are of great importance for achieving high-rate energy storage. Though these reports have studied the capacitive behaviour of 3D graphene networks in a three-electrode system or symmetric supercapacitor,[35–38] the studies on asymmetric supercapacitors are rarely reported. Therefore, preparing 3D graphene networks that combine high specific capacitance and good rate capability is highly expected for asymmetric supercapacitor applications.

In this paper, we develop an ASC using a hierarchical carbon nanotube@nickel hydroxide nanosheet (CNT@$Ni(OH)_2$) core–shell composite as the positive electrode and 3D graphene network (3DGN) as the negative electrode. The CNT@$Ni(OH)_2$ composites are prepared by a simple yet efficient chemical bath deposition method, while 3DGNs are obtained by freeze-drying of graphene hydrogels. The optimized CNT@$Ni(OH)_2$//3DGN ASC exhibits high energy density, high power density and acceptable cycling stability, indicating its huge potential for energy storage applications.

2. Experimental

2.1. Preparation of CNT@nickel hydroxide nanosheet (CNT@$Ni(OH)_2$) core–shell composites

The CNTs used in this study were purchased from Chengdu Organic Chemicals (Chengdu, China). In order to make the CNTs more dispersible in water, 1 g of CNTs were refluxed in HNO_3 (6 M, 50 mL) at 70 °C for 3 h, followed by washing with deionized water several times until neutral pH was obtained. Then the pretreated CNTs were dried at 60 °C overnight for further use.

Growing $Ni(OH)_2$ nanosheets on CNTs was realized by a facile chemical bath deposition process. In a typical procedure, 0.2 g of CNTs was dispersed in a 100 mL solution containing 0.025 mol of $Ni(NO_3)_2 \cdot 6H_2O$ and 0.5 mol urea by ultra-sonic agitation for 10 min. Then the mixture was heated at 80 °C for 2 h in an oil bath with stirring. After that, the solution was cooled down to room temperature naturally and aged for another 12 h. The final products, namely, CNT@$Ni(OH)_2$ composites, were collected by filtration and washed with deionized water and ethanol several times, and dried at 60 °C for 12 h. For comparison, a pure $Ni(OH)_2$ sample was prepared under the same conditions without CNTs.

2.2. Preparation of three-dimensional graphene networks (3DGNs)

3DGNs were prepared by freeze-drying of graphene hydrogels according to our previous work.[39] In a typical process, graphene oxide (GO) was firstly prepared from natural graphite flakes using a modified Hummers method.[40–42] Then 120 mg of GO was dispersed in 60 mL water by sonication for 1 h. The resulting mixture was sealed in a Teflon-lined autoclave and hydrothermally treated at 180 °C for 12 h to obtain the graphene hydrogels. After that, the obtained sample was freeze-dried overnight, followed by vacuum drying at 60 °C for 12 h.

2.3. Materials characterization

The morphologies of CNTs, CNT@$Ni(OH)_2$, and 3DGN were examined by field emission scanning electron microscopy (FESEM; Hitachi S-4800) and transmission electron microscopy (TEM; JEOL, JEM-2010). Powder X-ray diffraction (XRD) patterns of the as-prepared samples were recorded using a Bruker Focus D8 with Cu Kα radiation. Raman spectra were collected using a Renishaw Invia Raman microscope with a 514.5 nm laser under ambient conditions. The nitrogen adsorption–desorption isotherms were measured at 77 K using an automatic adsorption instrument (Tristar3000, Micromeritics).

2.4. Electrochemical measurements

A typical three-electrode experimental cell equipped with a working electrode, a platinum wire counter electrode, and a saturated calomel electrode (SCE) as the reference electrode was used for measuring the electrochemical properties of the working electrode. The electrolyte was a 1 M KOH aqueous solution. The working electrodes for tests were prepared by adding a few drops of ethanol to the mixture of active materials, acetylene black and polytetrafluoroethylene (PTFE) binder (weight ratio of 75 : 20 : 5) to form a homogeneous slurry. Then, the slurry was pressed onto the nickel foam current collector (1 cm × 1 cm) and dried at 120 °C for 12 h.

The electrochemical measurements of the asymmetric supercapacitor were performed in a two-electrode cell, where the CNT@$Ni(OH)_2$ positive electrode and 3DGN negative electrode were pressed together and separated by a polypropylene membrane separator. The electrolyte was a 1 M KOH aqueous

solution. The loading mass ratio of the active materials ($CNT@Ni(OH)_2$: 3DGN) was estimated to be 0.36 (1 cm × 1 cm; $CNT@Ni(OH)_2$ mass: ≈1 mg and 3DGN mass: ≈2.8 mg) from the specific capacitance and potential window obtained from their galvanostatic charge–discharge curves. All the electrochemical measurements were performed on a CHI 660D electrochemical workstation.

3. Results and discussion

3.1. Positive electrode materials

Fig. 1a gives the schematic illustration of the preparation process of $CNT@Ni(OH)_2$ composites. Ultrathin $Ni(OH)_2$ nanosheets are uniformly grown on the CNTs by a facile chemical bath deposition. During deposition the decomposition of urea releases ammonia and CO_2, which further react with water and nickel cations in the reaction solution to precipitate nanosheet-like $Ni(OH)_2$ on the surface of CNTs, leading to the formation of core–shell nanostructures. Fig. 1b–e show the FESEM images of CNTs and $CNT@Ni(OH)_2$ composites. CNTs reveal fibrous structures with a smooth surface and an outer diameter in the range of 20–60 nm. In the $CNT@Ni(OH)_2$ composites, the $Ni(OH)_2$ nanosheets are almost vertically grown on the individual CNT surface (Fig. 1d and e). A closer observation shows that the $Ni(OH)_2$ nanosheets are interconnected with one another (Fig. 1e), and such structures might exhibit better mechanical strength and form a better conductive network intimately contacted with the CNT core. At the same time, the interconnected $Ni(OH)_2$ nanosheets create a highly open and porous network, which can provide a high specific surface area and more active sites contacted with electrolyte ions, and accordingly realize the high utilization of the $Ni(OH)_2$ shell. In striking contrast, only aggregated micro-sized particles are observed in the pure $Ni(OH)_2$ sample (Fig. S1†). This demonstrates that the existence of CNTs is of great importance to form the $CNT@Ni(OH)_2$ core–shell composites, in which CNTs can not only serve as the conductive support for the growth of $Ni(OH)_2$ nanosheets, but also prevent the $Ni(OH)_2$ from aggregation.

The crystal phase and structural information of the products are analyzed using the X-ray diffraction (XRD) patterns as shown in Fig. 2. The CNTs show the characteristic graphitic (002) peak at 26° and (100) peak at 42.3°.[43] The XRD patterns of pure $Ni(OH)_2$ and $CNT@Ni(OH)_2$ exhibit the characteristic peaks of hexagonal $Ni(OH)_2$ (JCPDS, no. 22-0444) at 2θ = 11.6°, 23.8°,

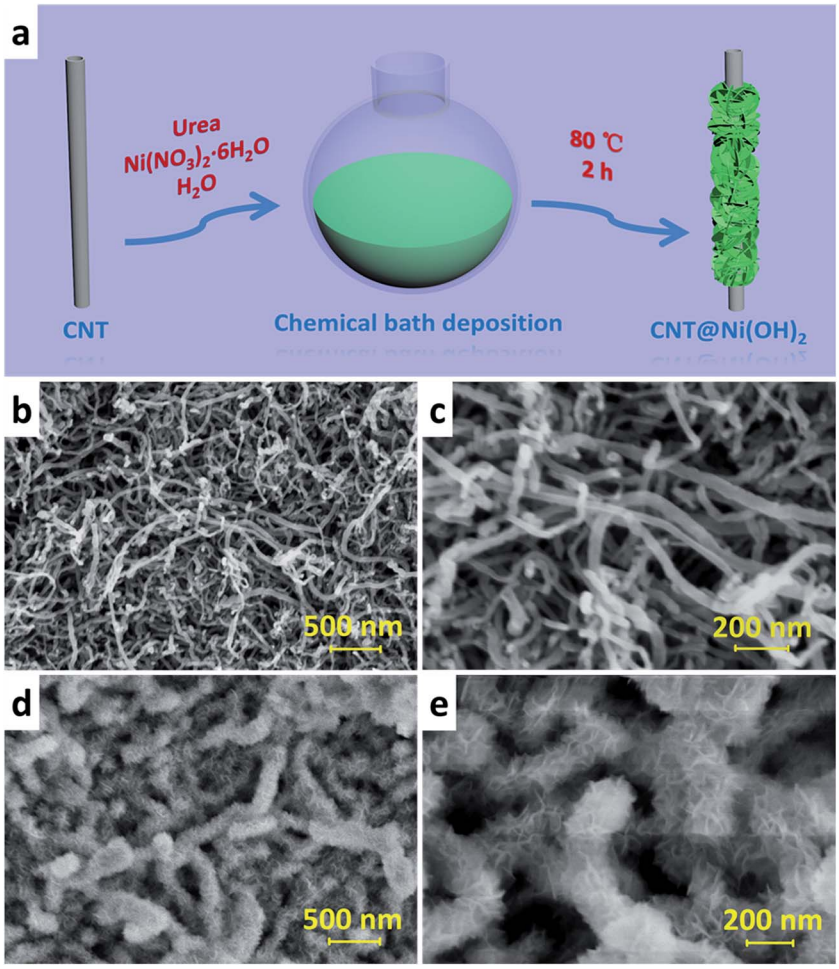

Fig. 1 (a) Schematic illustration of the preparation of $CNT@Ni(OH)_2$ composites. FESEM images of (b and c) CNTs and (d and e) $CNT@Ni(OH)_2$ composites.

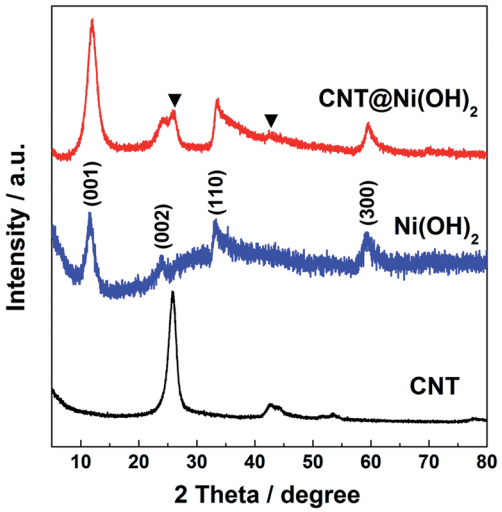

Fig. 2 XRD patterns of CNTs, pure $Ni(OH)_2$ and CNT@$Ni(OH)_2$ composites.

33.6° and 59.6°, corresponding to the (001), (002), (110) and (300) diffraction planes, respectively. Notice that the diffraction peaks of CNTs (marked by ▼) can also be observed in the CNT@$Ni(OH)_2$ composites, while the intensity is decreased compared with that of pure CNTs, implying the successful coating of $Ni(OH)_2$ nanosheets on CNTs.

The morphology and microstructure of CNTs and CNT@$Ni(OH)_2$ composites are further investigated by TEM. The CNTs show hollow tubular morphological features, and their outer diameters range between 20 and 60 nm (Fig. 3a). Fig. 3b and c display the TEM images of CNT@$Ni(OH)_2$ composites. It can be observed that the $Ni(OH)_2$ nanosheets fully cover the surface of CNTs, forming a core–shell nanostructure. As shown in the magnified TEM images (Fig. 3c and the inset), the $Ni(OH)_2$ nanosheets show a low contrast with the background (especially at the edges), indicating the ultrathin feature of these sheets. Thus, abundant exposed surfaces and full utilization of active materials could be expected, favorable for achieving a high specific capacitance. Fig. 3d shows the selected-area electron diffraction (SAED) pattern of the $Ni(OH)_2$ nanosheets. The SAED pattern shows well-defined diffraction rings, indicating the polycrystalline characteristics of the $Ni(OH)_2$ nanosheets. In addition, the diffraction rings from the inside to the outside can be indexed to the (110) and (300) planes of $Ni(OH)_2$, respectively. The SAED results are well in agreement with the above XRD analysis.

The capacitive behavior of the CNT@$Ni(OH)_2$ electrode was examined by cyclic voltammetry (CV) and galvanostatic charge–discharge (GCD) measurements in 1.0 M KOH aqueous electrolyte. Fig. 4a depicts the CV curves of CNT@$Ni(OH)_2$ composites, pure $Ni(OH)_2$, and CNT electrodes between a potential window of 0 and 0.6 V at a scan rate of 5 mV s^{-1}. Clearly, the current density of the CNT@$Ni(OH)_2$ electrode is

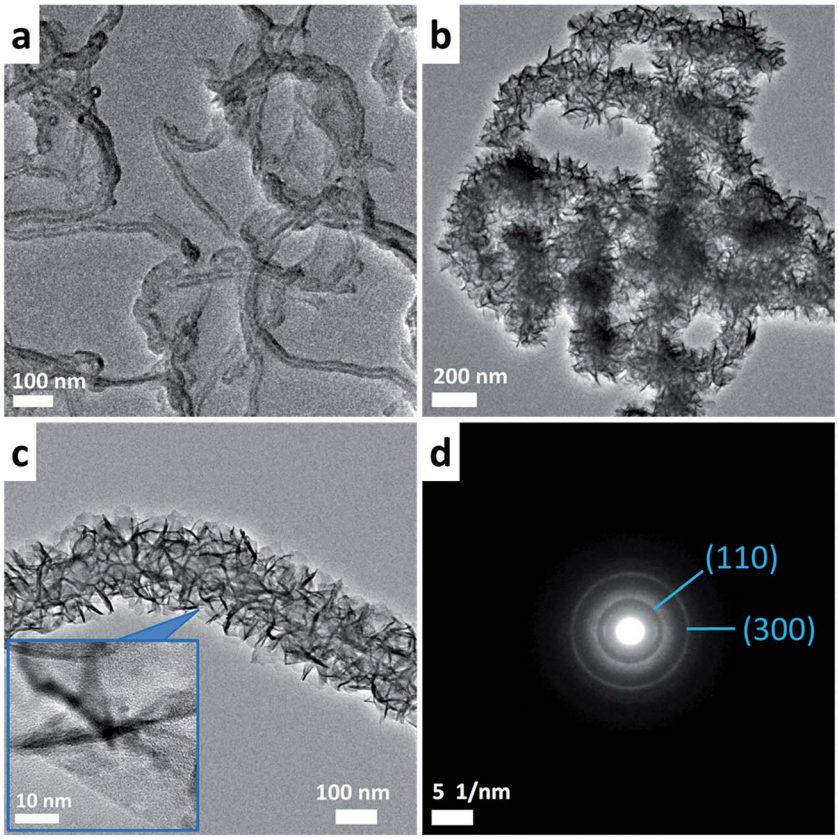

Fig. 3 TEM images of (a) CNTs and (b and c) CNT@$Ni(OH)_2$ composites. The inset of (c) gives the magnified TEM image of the $Ni(OH)_2$ nanosheet. (d) SAED pattern of CNT@$Ni(OH)_2$ composites.

much higher than those of CNTs and pure $Ni(OH)_2$. Because the specific capacitance is proportional to the area under the CV curve, the CNT@$Ni(OH)_2$ electrode shows a much larger charge storage capability than CNTs or pure $Ni(OH)_2$. Moreover, a pair of strong redox peaks can be observed in the CV curves of pure $Ni(OH)_2$ and CNT@$Ni(OH)_2$ electrodes. The redox peaks correspond to the reversible redox reaction of Ni(II) ↔ Ni(III), which can be described as:[4,5] $Ni(OH)_2 + OH^- \leftrightarrow NiOOH + H_2O + e^-$. Fig. 4b shows the CV curves of the CNT@$Ni(OH)_2$ composite electrode at different scan rates. When the scan rate increases (from 2 to 15 mV s^{-1}), the current response increases accordingly, and the shape of the CV curves is well-retained, indicating the superb rate capability of the CNT@$Ni(OH)_2$ electrode.

Fig. 4c compares the GCD curves of the CNT@$Ni(OH)_2$ composites with those of pure $Ni(OH)_2$ within a potential window of 0–0.5 V at 2 A g^{-1}. Obviously, the charging and discharging time of CNT@$Ni(OH)_2$ composites is much longer than that of pure $Ni(OH)_2$, suggesting the higher specific capacitance in the CNT@$Ni(OH)_2$ case. Fig. 4d shows the GCD curves of CNT@$Ni(OH)_2$ composites at different current densities. From the discharge curves, the specific capacitance can be calculated according to the equation: $C = I \times t/(\Delta V \times m)$, where C is the specific capacitance, I is the discharging current, t is the discharging time, ΔV is the potential drop during discharge, and m is the mass of active materials in a single electrode. Fig. 4e shows the calculated specific capacitances of CNT@$Ni(OH)_2$ composites and pure $Ni(OH)_2$ at various current densities. The specific capacitance of the CNT@$Ni(OH)_2$ composites at a current density of 2 A g^{-1} is as high as 1136 F g^{-1}, and even retains 384 F g^{-1} at a high current density of 20 A g^{-1}. In contrast, pure $Ni(OH)_2$ shows inferior capacitance performance (422 F g^{-1} at 2 A g^{-1} and 124 F g^{-1} at

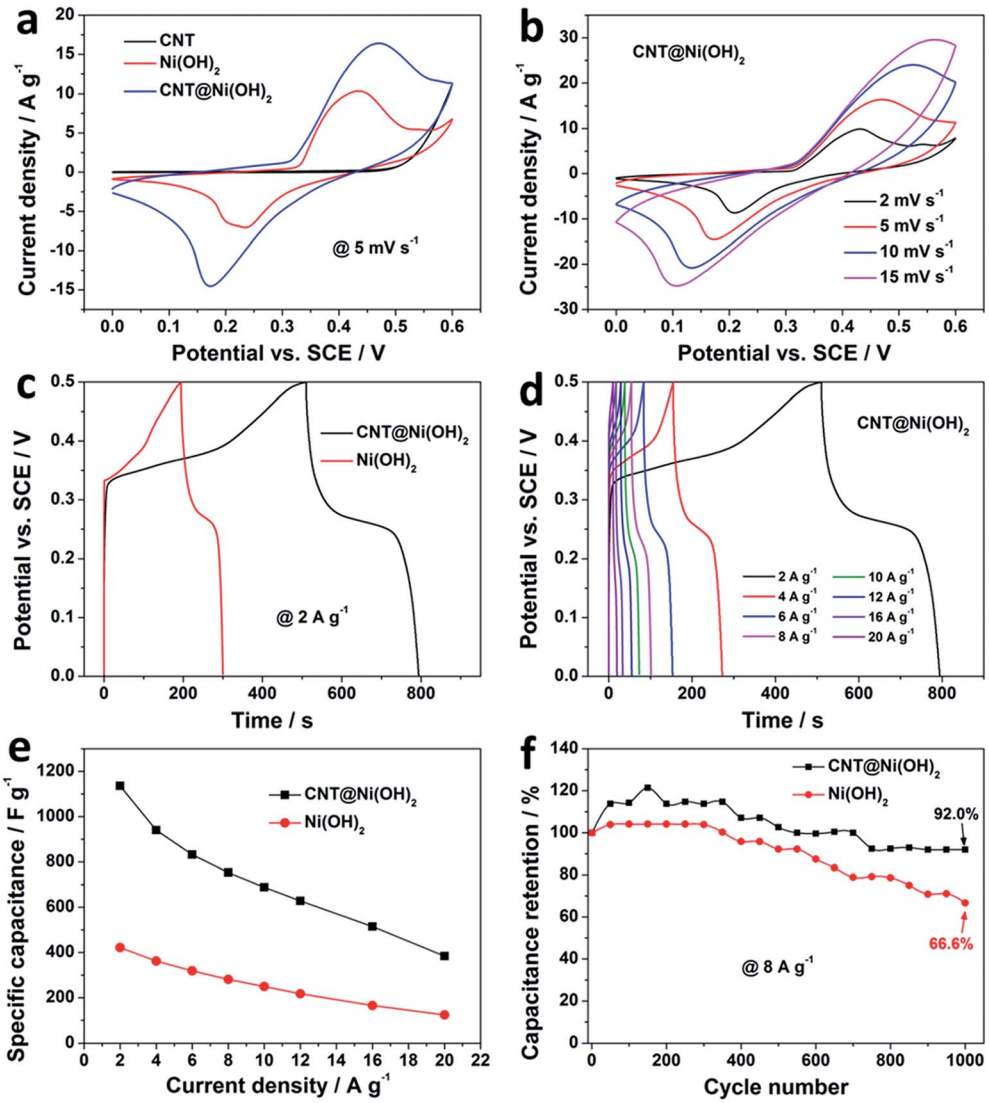

Fig. 4 CV curves of (a) CNTs, pure $Ni(OH)_2$ and CNT@$Ni(OH)_2$ composites at a scan rate of 5 mV s^{-1}, and (b) CNT@$Ni(OH)_2$ composites at various scan rates. GCD curves of (c) pure $Ni(OH)_2$ and CNT@$Ni(OH)_2$ composites at 2 A g^{-1} and (d) CNT@$Ni(OH)_2$ composites at various current densities. (e) Specific capacitance of pure $Ni(OH)_2$ and CNT@$Ni(OH)_2$ composites at different current densities. (f) Cycling performance of pure $Ni(OH)_2$ and CNT@$Ni(OH)_2$ composites at a current density of 8 A g^{-1}.

20 A g^{-1}). The capacitance retention from 2 to 20 A g^{-1} for CNT@$Ni(OH)_2$ is 33.8%, which is higher than that of pure $Ni(OH)_2$ (29.4%), confirming the enhanced rate capability of the CNT@$Ni(OH)_2$ composites. The much enhanced capacitance and improved rate capability of the CNT@$Ni(OH)_2$ composites can be attributed to the judiciously designed core–shell structure. The shell consisting of ultrathin $Ni(OH)_2$ nanosheets favors the fast faradic reaction, which endows the composites with high specific capacitance. Simultaneously, the highly conductive CNT core can serve as the "superhighway" for electron transport, which enables the good rate capability of the composites.

Long-term cycling performance is an important criterion for supercapacitors. To evaluate the cycling stabilities of CNT@$Ni(OH)_2$ composites and pure $Ni(OH)_2$, the charge–discharge cycling tests were performed at a high current density of 8 A g^{-1} for 1000 cycles. As shown in Fig. 4f, the specific capacitance of the CNT@$Ni(OH)_2$ composites increases in the first 150 cycles, which may be related to the activation of the electrode.[42] After 1000 cycles, the capacitance retention of CNT@$Ni(OH)_2$ composites is 92.0%, which is much higher than that of pure $Ni(OH)_2$ (66.6% retained after 1000 cycles). The comparison is made for SEM images of CNT@$Ni(OH)_2$ before and after 200 CV cycles (Fig. S3†), and the structure of the composite is well retained during charge–discharge cycling.

It is noticed that carbon nanotube/$Ni(OH)_2$ composites for supercapacitors have been reported (as listed in Table S4†). However the chemicals used in our experiments are simpler and safer and the synthesis condition in our work is mild (CBD at 80 °C for 2 h). More importantly, the nanostructures of the interconnected $Ni(OH)_2$ nanosheets are uniformly grown on the CNT surface forming CNT@$Ni(OH)_2$ core–shell composites, which are quite different from the reported results. Although the specific capacitance of CNT@$Ni(OH)_2$ in our work tested in a three-electrode system is slightly lower, given the method and chemicals used here are simpler and safer, these nanostructures are more competitive, and promising for large-scale synthesis.

3.2. Negative electrode materials

The fabrication process of the 3D graphene networks (3DGNs) is presented in Fig. 5a. Firstly, graphene oxide (GO) sheets were

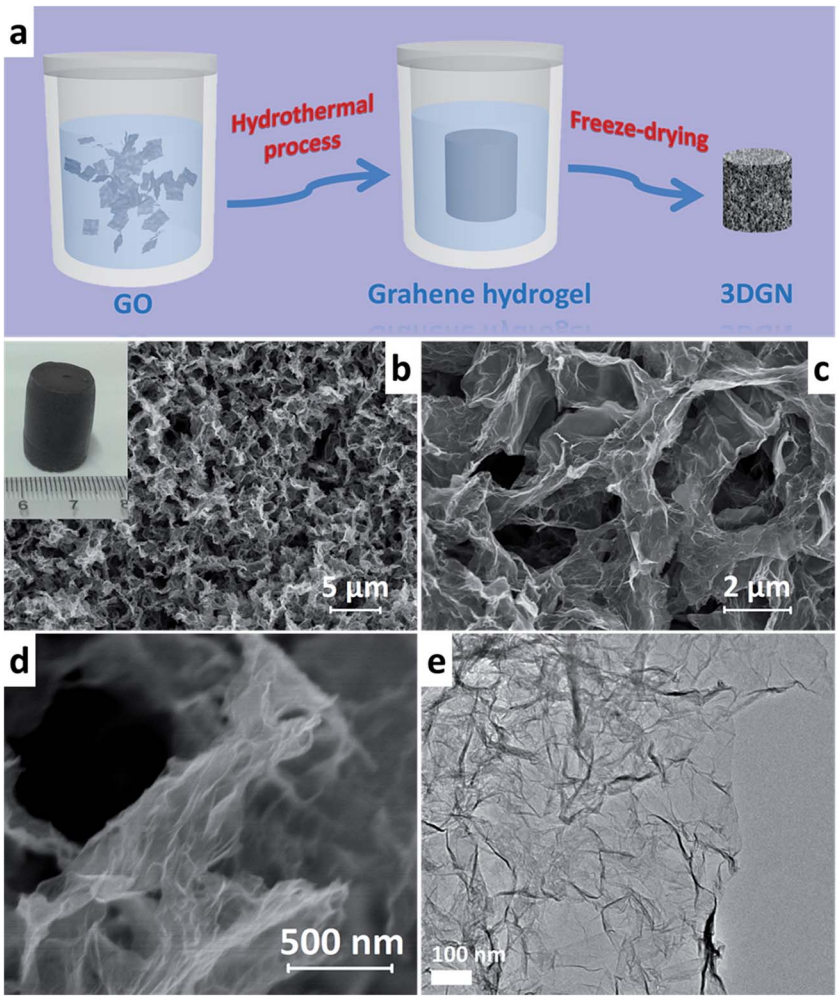

Fig. 5 (a) Schematic illustration of the preparation process of 3DGN. (b–d) FESEM images of 3DGN. The inset of (b) shows the photograph of 3DGN. (e) TEM image of 3DGN.

exfoliated to form a stable aqueous suspension. Subsequently, the suspension was hydrothermally treated to form a 3D graphene hydrogel as follows.[35,39] Before the hydrothermal reduction, the GO sheets are randomly dispersed in water owing to their hydrophilicity. When the GO sheets are hydrothermally reduced at 180 °C, they become regionally hydrophobic due to the decreased oxygenated functionalities. The combination of hydrophobicity, electrostatic repulsion, and π–π interactions causes a random cross-linking between flexible graphene sheets, which contribute to the formation of graphene hydrogels. Finally, the as-prepared graphene hydrogels were freeze-dried to remove entrapped water, whereby the 3D graphene networks (3DGNs) were obtained and tested as supercapacitor electrode materials. The inset of Fig. 5b shows the photograph of the monolithic structure of the 3DGN, which exhibits good mechanical strength to allow handling with tweezers and cutting with razor blades. The detailed microstructure of 3DGN was studied by FESEM and TEM. As shown in Fig. 5b, the 3DGN possesses a macroporous morphology on the whole. The magnified FESEM image (Fig. 5c) shows that 3DGNs are highly porous, three-dimensionally interconnected graphene networks with the pore sizes ranging from submicron to several microns. The pore walls are very thin and consist of crumpled, flexible, and ultrathin graphene sheets (Fig. 5c and d). Fig. 5e shows the TEM image of graphene sheets from the 3DGN that are almost transparent with some wrinkles demonstrating their ultrathin nature.

The 3DGNs are further characterized by XRD and Raman spectroscopy. The XRD pattern (Fig. 6a) shows two broad peaks at around 26° and 43° that can be assigned to the (002) and (100) diffraction peaks of graphene sheets, respectively. The Raman spectrum (Fig. 6b) shows four peaks, *i.e.*, the D band at 1350 cm^{-1}, the G band at 1580 cm^{-1}, the 2D band at 2680 cm^{-1} and the D + G band at 2920 cm^{-1}.[44,45] These Raman peaks

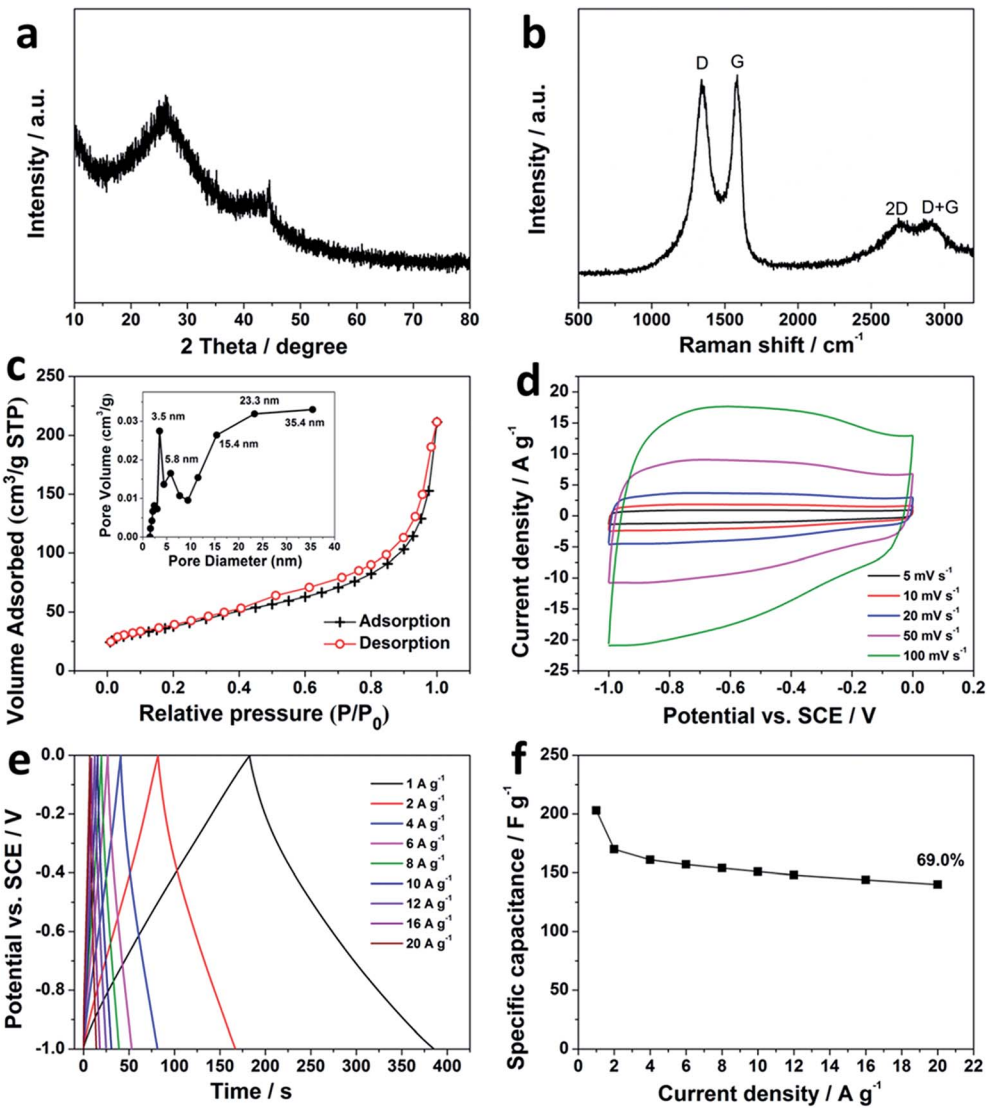

Fig. 6 (a) XRD pattern, (b) Raman spectrum and (c) N_2 adsorption–desorption isotherms of 3DGN. The inset of (c) shows the corresponding BJH pore size distribution for 3DGN. (d) CV curves of 3DGN at various scan rates. (e) GCD curves of 3DGN at various current densities. (f) Specific capacitance of 3DGN at different current densities.

indicate the carbon nature of the 3DGN. To study the pore structure of 3DGN, N_2 adsorption–desorption measurement was carried out at 77 K. Fig. 6c gives the N_2 adsorption–desorption isotherms of 3DGN, based on which the BET specific surface area is calculated to be 134.7 $m^2\ g^{-1}$ (Table S1†). Pore size distribution analysis using the Barrett–Joyner–Halenda (BJH) method shows that 3DGNs have a wide pore-size distribution from micropores to macropores (inset of Fig. 6c), which is consistent with the FESEM observations.

The CV curves of 3DGN at various scan rates are illustrated in Fig. 6d. When the scan rate increases from 5 to 100 mV s^{-1}, the CV curves retain a similar quasi-rectangular shape, indicating the ideal capacitive behavior of 3DGN and fast diffusion of electrolyte ions into the electrode. Fig. 6e shows the GCD curves of 3DGN at different current densities within a potential window of −1–0 V. From 1 to 20 A g^{-1}, all discharge curves are highly linear and symmetrical with their charge counterparts, demonstrating the excellent electrochemical reversibility of the 3DGN electrode. Fig. 6f shows the relationship between the specific capacitance and the current density for 3DGN. The specific capacitance reaches 203 F g^{-1} at 1 A g^{-1}. Even at a high current density of 20 A g^{-1}, the specific capacitance is still as high as 140 F g^{-1}, showing 69.0% retention relative to 1 A g^{-1}. Such capacitance retention indicates that 3DGN can provide reliable capacitive performance even during a rapid charge–discharge process. The excellent capacitive behavior of 3DGNs can be attributed to their unique structure. Firstly, the 3D porous structure effectively alleviates the restacking of graphene sheets and greatly increases the electrode/electrolyte contact area, resulting in an enhanced capacitance. Secondly, the hierarchical pores existing in 3DGN interconnected with each other provide a short diffusion distance and more ion

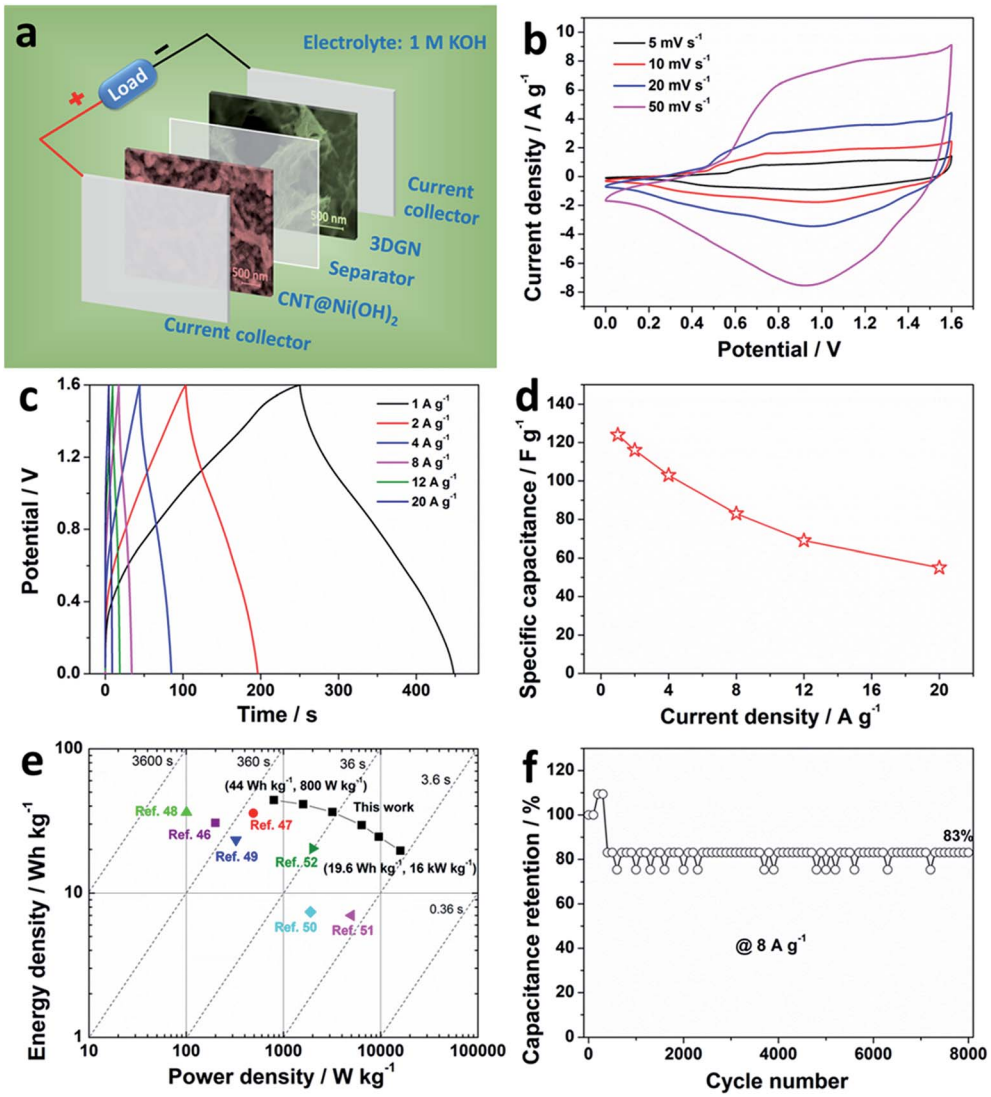

Fig. 7 (a) Schematic illustration of the assembled structure of the CNT@$Ni(OH)_2$//3DGN ASC. (b) CV curves of the CNT@$Ni(OH)_2$//3DGN ASC at various scan rates. (c) GCD curves of the CNT@$Ni(OH)_2$//3DGN ASC at various current densities. (d) Specific capacitance of the CNT@$Ni(OH)_2$//3DGN ASC at different current densities. (e) Ragone plot of the CNT@$Ni(OH)_2$//3DGN ASC. (f) Cycling performance of the CNT@$Ni(OH)_2$//3DGN ASC at a current density of 8 A g^{-1}.

channels, facilitating ion transportation. Thirdly, the cross-links of graphene sheets in 3DGN benefit the electron collection/transport between the graphene sheets, which is essential for achieving a high rate capability.

3.3. Asymmetric supercapacitors

Based on the CNT@Ni(OH)$_2$ composite (as the positive electrode) and 3DGN (as the negative electrode), the ASC is fabricated in a 1.0 M KOH aqueous electrolyte (Fig. 7a). To obtain an advanced supercapacitor, balancing the charges stored at the positive electrode (Q_+) and the negative electrode (Q_-) is important.[5] The charge (Q) stored by each electrode is related to the specific capacitance (C), the potential range for the charge–discharge process (ΔV), and the mass of the electrode (m), following the equation: $Q = C \times \Delta V \times m$. Given that $Q_+ = Q_-$, the mass ratio of positive and negative electrodes can be calculated by the equation: $m_+/m_- = (C_- \times \Delta V_-)/(C_+ \times \Delta V_+)$. In this study, the optimal mass ratio between the CNT@Ni(OH)$_2$ composite and 3DGN is expected to be m(CNT@Ni(OH)$_2$)/m(3DGN) = 0.36.

Fig. 7b shows the CV curves of the CNT@Ni(OH)$_2$//3DGN ASC at various scan rates in the potential range of 0–1.6 V, in which the broad redox peaks imply the pseudocapacitive feature of the CNT@Ni(OH)$_2$//3DGN ASC originating from the CNT@Ni(OH)$_2$ electrode. Fig. 7c presents the GCD curves at different current densities from 1 A g^{-1} to 20 A g^{-1}. No obvious IR drop is observed in all the discharge curves (the enlarged GCD curves at high current densities are shown in Fig. S2, ESI†), indicating the low internal resistance of the ASC. From the discharge curves, the specific capacitance values of the CNT@Ni(OH)$_2$//3DGN ASC are calculated based on the total mass of the active materials on the two electrodes (Fig. 7d and Table S2†). As shown in Fig. 7d, the specific capacitance reaches a maximum of 124 F g^{-1} at 1 A g^{-1}, and still retains 55 F g^{-1} when the current density increases 20 times (20 A g^{-1}, a full charge–discharge within 8.8 s). To further evaluate the energy storage performance of the CNT@Ni(OH)$_2$//3DGN ASC, Fig. 7e gives the Ragone plot, in which the energy density is plotted *versus* power density. Encouragingly, the energy density of the CNT@Ni(OH)$_2$//3DGN ASC can reach 44.0 W h kg^{-1} at a power density of 800 W kg^{-1}, and remains 19.6 W h kg^{-1} at a high power density of 16 000 W kg^{-1} (Fig. 7e and Table S2†). This surpasses many previously reported ASCs (more detailed test parameters are provided in Table S3†) including MnO$_2$/carbon nanofiber composites//activated carbon nanofibers (30.6 W h kg^{-1} at 200 W kg^{-1}),[46] Ni(OH)$_2$//activated carbon (35.7 W h kg^{-1} at 490 W kg^{-1}),[47] β-Ni(OH)$_2$/Ni-foam//activated carbon (36.2 W h kg^{-1} at 100.6 W kg^{-1}),[48] NiCo$_2$O$_4$-reduced graphite oxide//activated carbon (23.32 W h kg^{-1} at 324.9 W kg^{-1}),[49] Ni–Co oxide//activated carbon (7.4 W h kg^{-1} at 1902.9 W kg^{-1}),[50] MnO$_2$ nanowire/graphene//graphene (7.0 W h kg^{-1} at 5000 W kg^{-1}),[51] and V$_2$O$_5$·0.6H$_2$O nanoribbons//activated carbon (20.3 W h kg^{-1} at

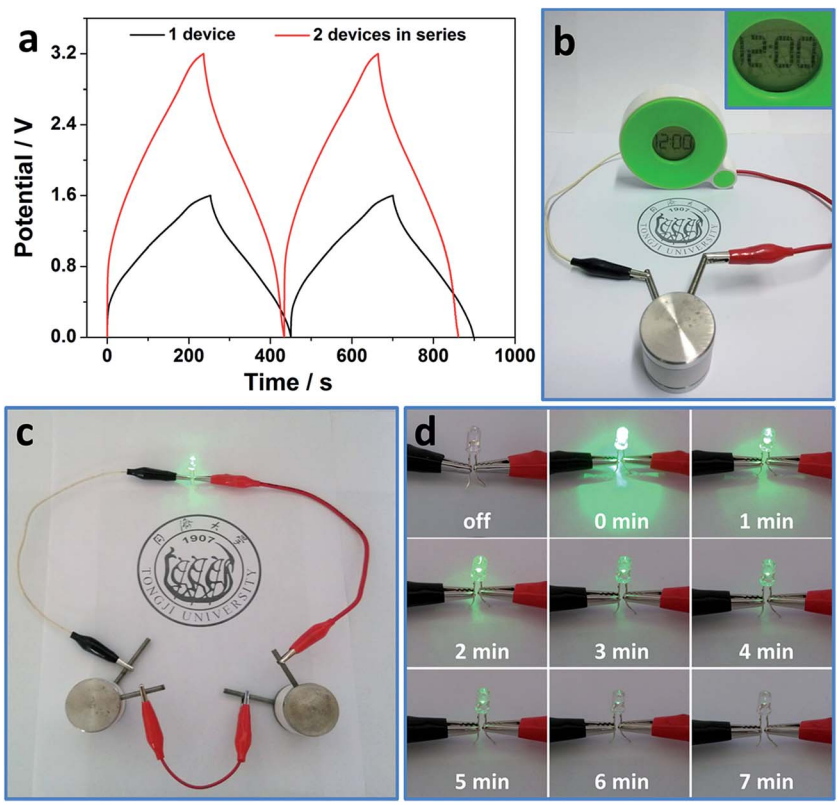

Fig. 8 (a) GCD curves of a single CNT@Ni(OH)$_2$//3DGN ASC device and two devices connected in series at a current of 3.8 mA. (b) Photograph of the CNT@Ni(OH)$_2$//3DGN ASC powering one digital clock (1.5 V). (c) Photograph of two CNT@Ni(OH)$_2$//3DGN ASCs connected in series powering one green LED (3–3.4 V). (d) Images of the green LED at different stages.

2000 W kg^{-1}).[52] Moreover, the electrochemical stability of the CNT@$Ni(OH)_2$//3DGN ASC was investigated by charge–discharge cycling at a current density of 8 A g^{-1}. As shown in Fig. 7f, the ASC exhibits capacitance retention of 83% after 8000 cycles, indicating the acceptable cycling stability and superiority to some previous ASCs, such as reduced graphene oxide–ruthenium oxide//reduced graphene oxide–polyaniline (70% retention after 2500 cycles),[53] $Ni(OH)_2$//activated carbon (82% retention after 1000 cycles),[54] graphene-MnO_2//graphene (less than 80% retention after 8000 cycles),[55] and MnO_2 nanowire/graphene//graphene (79% retention after 1000 cycles).[51]

Since a single ASC device has a limited working potential window, using serial assemblies would be a facile way to extend the operating voltage for high voltage output applications. Fig. 8a gives the GCD curves for a single CNT@$Ni(OH)_2$//3DGN ASC device and two devices connected in series tested at the same current (3.8 mA). The two ASC devices connected in series show a 3.2 V charge/discharge voltage with a similar discharge time compared with that of a single ASC with an operating voltage of 1.6 V, well following the theorem of series connections of capacitors. To evaluate the feasibility of the CNT@$Ni(OH)_2$//3DGN ASC, small electronic devices, such as a digital clock and light-emitting diode (LED), are driven by the as-prepared ASCs. Fig. 8b shows a digital clock with a working voltage of 1.5 V powered by one CNT@$Ni(OH)_2$//3DGN ASC. More interestingly, two ASCs in series can power one green LED (working voltage 3–3.4 V) after charging to 3.2 V (Fig. 8c and Video S1†). The LED can be lighted for more than 4 min as shown in Fig. 8d. These impressive results again confirm excellent performance of the CNT@$Ni(OH)_2$//3DGN ASC.

4. Conclusions

In summary, an advanced asymmetric supercapacitor has been constructed using carbon nanotube@nickel hydroxide nanosheet (CNT@$Ni(OH)_2$) core–shell composites and three-dimensional graphene networks (3DGNs) as the positive and negative electrodes, respectively. Benefiting from the high individual capacitive performance of CNT@$Ni(OH)_2$ and 3DGN, and the synergistic effects between the two electrodes, the CNT@$Ni(OH)_2$//3DGN ASC demonstrates excellent energy storage capability, namely, a high energy density (a maximum up to 44.0 W h kg^{-1}), high power density (a maximum up to 16 000 W kg^{-1}) and acceptable cycling stability (83% capacitance retention after 8000 cycles). These results not only indicate that the CNT@$Ni(OH)_2$//3DGN ASC holds great potential for energy storage applications, but also shed light on the importance of judiciously designed nanostructures for achieving enhanced performance.

Acknowledgements

The authors gratefully acknowledge the financial support offered by NSFC Grants (21173158, 21373152). Z. Guo appreciates the start-up funds from the University of Tennessee, Knoxville.

Notes and references

1 G. Wang, L. Zhang and J. Zhang, *Chem. Soc. Rev.*, 2012, **41**, 797.
2 P. Simon and Y. Gogotsi, *Nat. Mater.*, 2008, **7**, 845.
3 L. L. Zhang and X. S. Zhao, *Chem. Soc. Rev.*, 2009, **38**, 2520.
4 Z. Tang, C.-h. Tang and H. Gong, *Adv. Funct. Mater.*, 2012, **22**, 1272.
5 J. Yan, Z. Fan, W. Sun, G. Ning, T. Wei, Q. Zhang, R. Zhang, L. Zhi and F. Wei, *Adv. Funct. Mater.*, 2012, **22**, 2632.
6 H. Gao, F. Xiao, C. B. Ching and H. Duan, *ACS Appl. Mater. Interfaces*, 2012, **4**, 2801.
7 F. Wang, S. Xiao, Y. Hou, C. Hu, L. Liu and Y. Wu, *RSC Adv.*, 2013, **3**, 13059.
8 H. Wang, C. M. B. Holt, Z. Li, X. Tan, B. S. Amirkhiz, Z. Xu, B. C. Olsen, T. Stephenson and D. Mitlin, *Nano Res.*, 2012, **5**, 605.
9 H. Wang, Q. Gao and J. Hu, *J. Power Sources*, 2010, **195**, 3017–3024.
10 C.-C. Hu, J.-C. Chen and K.-H. Chang, *J. Power Sources*, 2013, **221**, 128.
11 M. Zhi, C. Xiang, J. Li, M. Li and N. Wu, *Nanoscale*, 2013, **5**, 72.
12 H. Wang, H. S. Casalongue, Y. Liang and H. Dai, *J. Am. Chem. Soc.*, 2010, **132**, 7472.
13 J. Liang, B. Dong, S. Ding, C. Li, B. Q. Li, J. Li and G. Yang, *J. Mater. Chem. A*, 2014, **2**, 11299.
14 X. A. Chen, X. Chen, F. Zhang, Z. Yang and S. Huang, *J. Power Sources*, 2013, **243**, 555.
15 L. L. Zhang, Z. Xiong and X. S. Zhao, *J. Power Sources*, 2013, **222**, 326.
16 R. R. Salunkhe, J. Lin, V. Malgras, S. X. Dou, J. H. Kim and Y. Yamauchi, *Nano Energy*, 2015, **11**, 211.
17 S. Chen, J. Zhu, H. Zhou and X. Wang, *RSC Adv.*, 2011, **1**, 484.
18 Q. Huang, X. Wang, J. Li, C. Dai, S. Gamboa and P. J. Sebastian, *J. Power Sources*, 2007, **164**, 425.
19 J. H. Park, O. O. Park, K. H. Shin, C. S. Jin and J. H. Kim, *Electrochem. Solid-State Lett.*, 2002, **5**, H7.
20 S. Yang, X. Wu, C. Chen, H. Dong, W. Hu and X. Wang, *Chem. Commun.*, 2012, **48**, 2773.
21 B. Dong, H. Zhou, J. Liang, L. Zhang, G. Gao and S. Ding, *Nanotechnology*, 2014, **25**, 435403.
22 Y. Xu, X. Huang, Z. Lin, X. Zhong, Y. Huang and X. Duan, *Nano Res.*, 2013, **6**, 65.
23 H. Wang, Y. Liang, T. Mirfakhrai, Z. Chen, H. S. Casalongue and H. Dai, *Nano Res.*, 2011, **4**, 729–736.
24 H. Yan, J. Bai, B. Wang, L. Yu, L. Zhao, J. Wang, Q. Liu, J. Liu and Z. Li, *Electrochim. Acta*, 2015, **154**, 9.
25 G. W. Yang, C. L. Xu and H. L. Li, *Chem. Commun.*, 2008, 6537.
26 Z. Lu, Z. Chang, W. Zhu and X. Sun, *Chem. Commun.*, 2011, **47**, 9651.
27 I. Dumitrescu, P. R. Unwin and J. V. Macpherson, *Chem. Commun.*, 2009, 6886.
28 J. M. Schnorr and T. M. Swager, *Chem. Mater.*, 2011, **23**, 646.

29 X. Chen, H. Zhu, Y.-C. Chen, Y. Shang, A. Cao, L. Hu and G. W. Rubloff, *ACS Nano*, 2012, **6**, 7948.
30 Y. Hou, L. Chen, P. Liu, J. Kang, T. Fujita and M. Chen, *J. Mater. Chem. A*, 2014, **2**, 10910.
31 J. Chen, C. Li and G. Shi, *J. Phys. Chem. Lett.*, 2013, **4**, 1244.
32 Y. Huang, J. Liang and Y. Chen, *Small*, 2012, **8**, 1805.
33 D. Li, M. B. Muller, S. Gilje, R. B. Kaner and G. G. Wallace, *Nat. Nanotechnol.*, 2008, **3**, 101.
34 X. Yang, J. Zhu, L. Qiu and D. Li, *Adv. Mater.*, 2011, **23**, 2833.
35 Y. Xu, K. Sheng, C. Li and G. Shi, *ACS Nano*, 2010, **4**, 4324.
36 Y. Xu, Z. Lin, X. Huang, Y. Wang, Y. Huang and X. Duan, *Adv. Mater.*, 2013, **25**, 5779.
37 L. Zhang and G. Shi, *J. Phys. Chem. C*, 2011, **115**, 17206.
38 Z. S. Wu, Y. Sun, Y. Z. Tan, S. Yang, X. Feng and K. Mullen, *J. Am. Chem. Soc.*, 2012, **134**, 19532.
39 H. Wang, C. Guan, X. Wang and H. J. Fan, *Small*, 2015, **11**, 1470.
40 W. S. Hummers and R. E. Offeman, *J. Am. Chem. Soc.*, 1958, **80**, 1339.
41 H.-W. Wang, Z.-A. Hu, Y.-Q. Chang, Y.-L. Chen, Z.-Q. Lei, Z.-Y. Zhang and Y.-Y. Yang, *Electrochim. Acta*, 2010, **55**, 8974.
42 H.-W. Wang, Z.-A. Hu, Y.-Q. Chang, Y.-L. Chen, H.-Y. Wu, Z.-Y. Zhang and Y.-Y. Yang, *J. Mater. Chem.*, 2011, **21**, 10504.
43 B. Gao, C.-Z. Yuan, L.-H. Su, L. Chen and X.-G. Zhang, *J. Solid State Electrochem.*, 2008, **13**, 1251.
44 M. M. Kadam, O. R. Lokare, K. V. M. K. Kireeti, V. G. Gaikar and N. Jha, *RSC Adv.*, 2014, **4**, 62737.
45 P. Wen, P. Gong, Y. Mi, J. Wang and S. Yang, *RSC Adv.*, 2014, **4**, 35914.
46 J.-G. Wang, Y. Yang, Z.-H. Huang and F. Kang, *Carbon*, 2013, **61**, 190.
47 H. B. Li, M. H. Yu, F. X. Wang, P. Liu, Y. Liang, J. Xiao, C. X. Wang, Y. X. Tong and G. W. Yang, *Nat. Commun.*, 2013, **4**, 1894.
48 J. Huang, P. Xu, D. Cao, X. Zhou, S. Yang, Y. Li and G. Wang, *J. Power Sources*, 2014, **246**, 371.
49 X. Wang, W. S. Liu, X. Lu and P. S. Lee, *J. Mater. Chem.*, 2012, **22**, 23114.
50 C. Tang, Z. Tang and H. Gong, *J. Electrochem. Soc.*, 2012, **159**, A651.
51 Z.-S. Wu, W. Ren, D.-W. Wang, F. Li, B. Liu and H.-M. Cheng, *ACS Nano*, 2010, **4**, 5835.
52 Q. T. Qu, Y. Shi, L. L. Li, W. L. Guo, Y. P. Wu, H. P. Zhang, S. Y. Guan and R. Holze, *Electrochem. Commun.*, 2009, **11**, 1325.
53 J. Zhang, J. Jiang, H. Li and X. S. Zhao, *Energy Environ. Sci.*, 2011, **4**, 4009.
54 J.-W. Lang, L.-B. Kong, M. Liu, Y.-C. Luo and L. Kang, *J. Solid State Electrochem.*, 2009, **14**, 1533.
55 L. Deng, G. Zhu, J. Wang, L. Kang, Z.-H. Liu, Z. Yang and Z. Wang, *J. Power Sources*, 2011, **196**, 10782.